

# The molecular gas content of the advanced S+E merger NGC 4441

## Evidence for an extended decoupled nuclear disc?

E. Jütte<sup>1,2</sup>, S. Aalto<sup>3</sup>, and S. Hüttemeister<sup>1</sup>

<sup>1</sup> Astronomisches Institut der Ruhr-Universität Bochum, 44780 Bochum, Germany

<sup>2</sup> Astron, 7990AA Dwingeloo, The Netherlands

<sup>3</sup> Onsala Space Observatory, Chalmers University of Technology, SE-439 92 Onsala, Sweden

Received ; accepted

### ABSTRACT

**Context.** Mergers between a spiral and an elliptical (S+E mergers) are poorly studied so far despite the importance for galaxy evolution. NGC 4441 is a nearby candidate for an advanced remnant of such a merger, showing typical tidal structures like an optical tail and two shells as well as two H I tails.

**Aims.** The study of the molecular gas content gives clues on the impact of the recent merger event on the star formation. Simulations of S+E mergers predict contradictory scenarios concerning the strength and the extent of an induced starburst. Thus, observations of the amount and the distribution of the molecular gas, the raw material of star formation, are needed to understand the influence of the merger on the star formation history.

**Methods.** <sup>12</sup>CO and <sup>13</sup>CO (1-0) and (2-1) observations were obtained using the Onsala Space Observatory 20 m and IRAM 30 m telescope as well as the Plateau de Bure interferometer. These data allow us to carry out a basic analysis of the molecular gas properties such as estimates of the molecular gas mass, its temperature and density and the star formation efficiency.

**Results.** The CO observations reveal an extended molecular gas reservoir out to  $\sim 4$  kpc, with a total molecular gas mass of  $\sim 5 \cdot 10^8 M_{\odot}$ . Furthermore, high resolution imaging shows a central molecular gas feature, most likely a rotating disc hosting most of the molecular gas ( $\sim 4 \cdot 10^8 M_{\odot}$ ). This nuclear disc shows a different sense of rotation than the large-scale H I structure, indicating a kinematically decoupled core. We modeled the state of the interstellar medium with the radiative transfer code RADEX, using the ratios of the <sup>12</sup>CO and <sup>13</sup>CO lines. The results are consistent with a diffuse ( $n \leq 10^3 \text{ cm}^{-3}$ ) molecular medium with no significant indications for cold and dense cores of ongoing star formation. This is in agreement with the moderate star formation rate of  $1 - 2 M_{\odot} \text{ yr}^{-1}$  found in NGC 4441. Under the assumption of a constant star formation rate, the gas depletion time is  $\tau = 4.8 \cdot 10^8 \text{ yr}$ . NGC 4441 might be a nearby candidate for an early-type galaxy with a dominating A star population, a so-called E+A galaxy, being in a poststarburst phase several  $10^8 \text{ yr}$  after a merger event.

**Key words.** galaxies: interactions – galaxies: starburst – galaxies: individual: NGC 4441 – radio lines: galaxies – radio lines: ISM

## 1. Introduction

Following the  $\Lambda$ CDM models for galaxy evolution, mergers between galaxies occur frequently and are essential to form the large galaxies we see today (e.g., Steinmetz 2003). While most observational studies concentrate on mergers between two spiral galaxies, simulations by Naab & Burkert (2000), Naab & Burkert (2001), Khochfar & Burkert (2003) and Naab et al. (2006) revealed the importance of mergers between a spiral and an elliptical (so-called S+E mergers) for the formation of bright ellipticals. Observations of this class of mergers are needed to investigate their relevance and influence on galaxy evolution.

The well studied major mergers of two gas-rich disc galaxies can lead to ultraluminous infrared galaxies (ULIRGs,  $L_{\text{FIR}} > 10^{12} L_{\odot}$ , Sanders & Mirabel (1996)) because of a merger-induced extreme starburst. S+E mergers are however poorly studied so far and thus, it is unclear if starbursts generally occur in these mergers and how they evolve. Besides the lack of observations, models of S+E mergers are in strong disagreement

concerning the prediction of interaction-triggered enhanced star formation. Weil & Hernquist (1993) predict a congregation of the gas in the center of the remnant galaxy, leading to a strong gas concentration and thus resulting in a starburst, similar to ULIRGs but less intense. Simulations by Kojima & Noguchi (1997) however predict a dispersion of gas clouds which might not lead to a starburst at all, because the density of the gas is too low for it to collapse and form new stars. For the understanding of galaxy evolution it is necessary to know which scenario is more realistic and in particular how S+E mergers influence the stellar population content in the remnant. Observations of the molecular gas can show the amount and extent of raw material for star formation. Investigations of the molecular gas content in interacting galaxies showed a concentration of the gas towards the centre and an increase of the gas mass compared to non-interacting galaxies (e.g., Braine & Combes 1992, 1993; Horellou & Booth 1997). In ULIRGs, the molecular gas forms compact nuclear rotating rings and discs, fueling the central starburst (e.g., Bryant & Scoville 1996; Downes & Solomon 1998; Bryant & Scoville 1999; Greve et al. 2006). It is not known so far whether this is also the case in S+E mergers.

**Table 1.** Basic properties of NGC 4441. The distance is based on  $H_0 = 75 \text{ km s}^{-1} \text{ Mpc}^{-1}$ .

<sup>b</sup> The Hubble type is taken from de Vaucouleurs et al. (1995)

<sup>b</sup> taken from Manthey et al. (2008a).

property	
RA (2000)	12:27:20.3
DEC (2000)	+64:48:05
$v_{\text{opt, hel}}$ (km s <sup>-1</sup> )	2722
$D$ (Mpc)	36
type <sup>a</sup>	SAB0+ pec
$L_B$ ( $10^9 L_\odot$ )	10.1
$L_{\text{FIR}}$ ( $10^9 L_\odot$ )	5.4
$\text{SFR}_{\text{FIR}}$ ( $M_\odot$ )	1.0
$\text{SFR}_{20\text{cm}}^b$ ( $M_\odot$ )	2.4
$l'$	10.5 kpc

One 'prototypical' S+E merger candidate is NGC 4194, the Medusa. In the optical we see a diffuse tail going to the north and on the opposite side two stellar shells are visible, consistent with predictions. Molecular gas is found out to 4.7 kpc away from the center, i.e. much more spread out than in the case of a ULIRG (Aalto & Hüttemeister 2000; Aalto et al. 2001). However, this galaxy is clearly undergoing an intense starburst phase, albeit not as intense as in ULIRGs (Weistrop et al. 2004). Here we present CO maps of another S+E merger candidate, NGC 4441 (see Table 1) (see discussion of merger history in Manthey et al. 2008a). The optical morphology of this galaxy is very similar to the Medusa. It possesses one tidal tail and two bright shells on the opposite side which is typical for S+E merger remnants (e.g., Quinn 1984; Dupraz & Combes 1985; Kojima & Noguchi 1997). The main body has an elliptical shape (Bergvall 1981) with a small dust lane through the center along the minor axis. In contrast to the strong similarities in the optical morphology compared with the Medusa, the atomic gas distribution is significantly different, since the H I forms two symmetric tidal tails (compared to only one tail in the Medusa (Manthey et al. 2008b)). In NGC 4441, the total H I mass is  $1.5 \cdot 10^9 L_\odot$  (Manthey et al. 2008a). The ongoing star formation rate is rather low ( $1 - 2 M_\odot \text{ yr}^{-1}$ ), because the merger is in such an advanced phase that most of the gas has been already used for star formation (Manthey et al. 2005, 2008a). Using optical spectra Bergvall (1981) found indications for a period of enhanced star formation in the past, since the stellar population is younger than that of a normal elliptical galaxy. Our own optical spectra confirm this and we estimate that a moderate starburst occurred  $\sim 1 \text{ Gyr}$  ago (Manthey et al. 2005).

## 2. Observations & data reduction

### 2.1. Onsala Space Observatory 20 m

First  $^{12}\text{CO}(1-0)$  observations were carried out in March 2003 using the 20 m telescope of the Onsala Space Observatory (OSO), Sweden. CO observations were done with a SIS-mixer and a correlator with a total bandwidth of 512 MHz. The main beam efficiency at 115 GHz is  $\eta = 0.43$ . To account for the highly variable sky background, the observations were done in the beam switching mode. The switching frequency was 1.8 Hz and the beam throw  $11'$ . We observed the center position as given in Table 1 under good weather conditions, i.e. 30% humidity and clear, stable sky. The pointing and focus was regularly checked

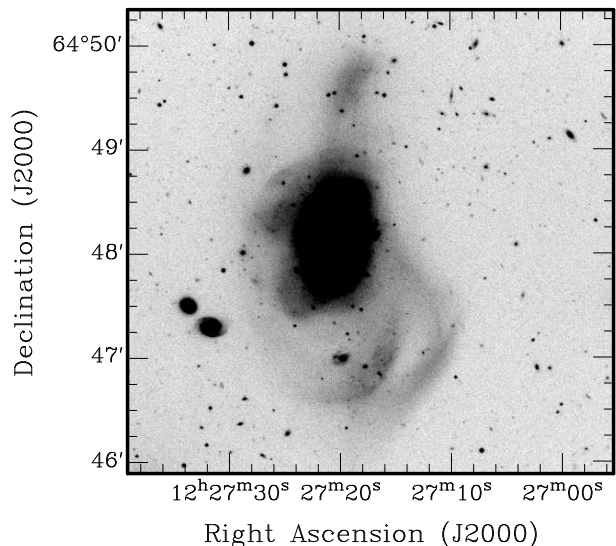


**Fig. 1.** R-Band image of NGC 4441, observed with the Calar Alto 2.2 m, integration time 1 h (Jütte et al. 2009). Note the tidal tail to the north and two stellar shells to the south-west. The two galaxies south-east of the main body are background galaxies.

during the observations with the calibration sources R Leo and R Cas. Table 2 summarises the observations.

### 2.2. IRAM 30 m

Follow-up CO observations of NGC 4441 were done with the IRAM 30 m telescope on Pico Veleta, Spain in July 2004. The weather conditions were good. We mapped an extended CO distribution both in the  $^{12}\text{CO}(1-0)$  and  $(2-1)$  line. We used the A 100 and B 100 as well as the A 230 and B 230 receivers to observe the  $^{12}\text{CO}(1-0)$  and  $(2-1)$  lines simultaneously. The 1 MHz filterbank with  $2 \times 512$  channels was chosen as a backend. The observations were done in beam switching mode. Pointing and focus calibration were regularly checked by observing Saturn. As a second pointing source near NGC 4441, we observed the calibration source 0954+658. To get a proper spatial coverage (a fully sampled map) even in the  $^{12}\text{CO}(2-1)$  line, we mapped the center using a  $3 \times 3$  grid with a spacing of  $6''$ , i.e. half the width of the  $^{12}\text{CO}(2-1)$  beam. For the outer positions, we used steps of  $22''$  (full  $^{12}\text{CO}(1-0)$  beamwidth) to cover a larger area, since we wanted to track the extent of the molecular gas. In total, we observed 17 positions out to  $44''$ . In the most distant pointings we do not find emission any more, thus, we covered the central molecular gas extent completely and are able to estimate source size and total mass.

The central position was also observed in  $^{13}\text{CO}$  with the  $(1-0)$  and  $(2-1)$  transitions being measured simultaneously.

### 2.3. Plateau de Bure

To map the CO distribution at higher spatial resolution we obtained interferometric observations in December 2005, May and July 2007 using the Plateau de Bure interferometer (PdBI). The observations were done with a dual polarization receiver covering a bandwidth of 4 GHz with 240 channels and centered at the redshifted  $\text{CO}(1-0)$  line at 114.252 GHz. This leads to a resolution of  $6.56 \text{ km s}^{-1}$ . The beamsize was  $3.25'' \times 2.65''$ , the position angle  $122^\circ$ . The primary beam at 115 GHz is  $45''$ . In total, we had an integration time of 16 hours on source. The observa-

**Table 2.** Parameters for the CO observations of NGC 4441 with the OSO 20 m and IRAM 30 m telescopes as well as the Plateau de Bure interferometer. The velocity resolution is given as a smoothed one, which is used throughout this paper.

obs. parameters	IRAM 30 m	OSO 20 m	PdB
$T_{\text{sys}}$ (K)	200-340 ( $^{12}\text{CO}$ ) ~ 145 ( $^{13}\text{CO}$ )	~ 350	180
$\theta_{\text{beam}}$ CO(1-0)	22''	33''	3.25''
$\theta_{\text{beam}}$ CO(2-1)	11''	–	–
$\Delta v$ CO(1-0)	21.0 km s $^{-1}$	33.8 km s $^{-1}$	6.6
$\Delta v$ CO(2-1)	21.0 km s $^{-1}$	–	–
$\eta$	0.75 (1-0) / 0.52 (2-1)	0.43	0.6-0.9

tions were done with the 6Cq–E10, 5Dq–W05 and 5Dq configurations. Flux, phase, and bandpass calibrators were 1044+719, 0418+380, 3C 273, and 3C 454.

#### 2.4. Data reduction

The CLASS<sup>1</sup> package was used for the data reduction at Onsala; the IRAM CO data were reduced using XS<sup>2</sup>, a graphical reduction and analysis software for mm spectral line data written by P. Bergman. After checking the quality of each single spectrum, the data were averaged with a weighting based on the system temperature and integration time. A first-order baseline was fitted to the resulting spectrum and subtracted. The data were converted to main beam brightness temperature ( $T_{\text{MB}}$ ) using the beam efficiencies given in Table 2. Finally, we smoothed the spectra to a velocity resolution of 21 km s $^{-1}$  (IRAM) and 34 km s $^{-1}$  (OSO), respectively, to achieve a better signal-to-noise ratio in individual channels. For the different positions in the  $^{12}\text{CO}(1-0)$  map we reached a noise level of 1.6–5.3 mK, in the  $^{12}\text{CO}(2-1)$  map the noise level lies between 2.1 and 9.6 mK  $T_{\text{MB}}$ . For  $^{13}\text{CO}$ , noise levels are 0.7 mK (1-0) and 1.3 mK (2-1).

The Plateau de Bure data were reduced using the GILDAS task CLIC. After flagging and phase and flux calibration using the observed calibrator sources, a uv-table of the science data was created. The uv-table was then transformed into a map using a natural weighting scheme. This dirty map was CLEANed to correct for sidelobes. After CLEANing, the rms noise level in the cube is 2.9 mJy beam $^{-1}$ . Finally, moment maps were created from the CLEANed cubes using a clip value of  $4\sigma = 0.012 \text{ Jy beam}^{-1}$ .

## 3. Results

### 3.1. CO distribution and molecular mass

First OSO observations revealed a molecular gas content in the inner 33'' of  $\sim 4.7 \times 10^8 M_{\odot}$ . The mass was derived by calculating the  $\text{H}_2$  column density

$$N(\text{H}_2) = X_{\text{CO}} \cdot \int I_{\text{CO}} dv \text{ cm}^{-2} \quad (1)$$

and thus

$$M_{\text{H}_2} = N(\text{H}_2) \cdot m(\text{H}_2) \cdot \Omega M_{\odot} \quad (2)$$

<sup>1</sup> Continuum and Line Analysis Single-dish Software, <http://www.iram.fr/IRAMFR/GILDAS/>

<sup>2</sup> <ftp://yggdrasil.oso.chalmers.se/pub/xs/>

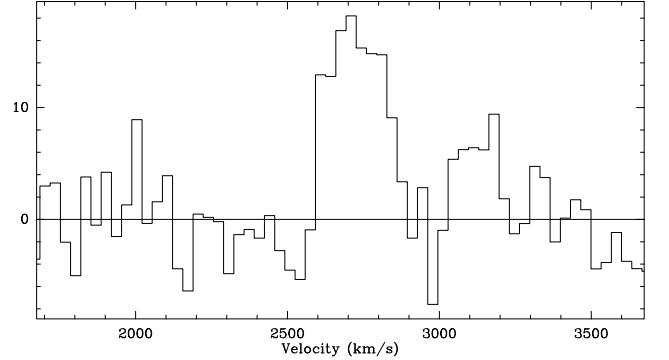


**Fig. 2.**  $^{12}\text{CO}(1-0)$  spectrum observed with the OSO 20 m telescope. The intensity is given in  $T_{\text{MB}}$  (mK).

with  $X_{\text{CO}}$  the CO- $\text{H}_2$  conversion factor,  $I_{\text{CO}}$  the intensity of the CO line in Kelvin,  $m(\text{H}_2)$  the mass of an  $\text{H}_2$  molecule in kg and  $\Omega$  the area covered by the beam in linear scales ( $\text{cm}^2$ ). We used a 'standard' conversion factor of  $X_{\text{CO}} = 2.3 \cdot 10^{20} \text{ cm}^{-2} (\text{K km s}^{-1})^{-1}$ , referring to Strong et al. (1988). Fig. 2 shows the observed CO spectrum.

Mapping NGC 4441 in CO with the IRAM 30 m telescope, we found a molecular gas distribution extended in particular to the south-east. Table 3 gives the pointings relative to the center position, the noise levels, the widths determined from Gaussians of both the  $^{12}\text{CO}(1-0)$  and CO(2-1) lines and the integrated intensities. In Fig. 3 and Fig. 4 we present the spectra of the mapped positions for both the  $^{12}\text{CO}(1-0)$  and CO(2-1) lines.

Under the assumption of a Gaussian distribution of the intensity, we plotted the intensity versus radial distance from the center and fitted a Gaussian to derive the source size (see Fig. 5 for  $^{12}\text{CO}(1-0)$ ). The real source size can be estimated from the observed source size and the known beam size as  $\Theta_{\text{source}}^2 = \Theta_{\text{obs}}^2 - \Theta_{\text{beam}}^2$ . We derive a deconvolved source size of  $\text{FWHM}^3 = 22'' \pm 1''$  (3.9 kpc) for  $^{12}\text{CO}(1-0)$ . The estimated source size for  $^{12}\text{CO}(2-1)$  is slightly larger ( $30'' \pm 3''$ ), but this is probably an artefact due to undersampling of the source coverage and lower signal-to-noise ratios in this transition. In our further discussion, we assume an identical extent of  $^{12}\text{CO}(2-1)$  and (1-0). We determined a central  $\text{H}_2$  column density of  $1.8 \cdot 10^{21} \text{ cm}^{-2}$  and calculated a total molecular gas mass of  $4.6 \cdot 10^8 M_{\odot}$ , according to equations (1) and (2).

Since we found extended gas to the south and east (see Fig. 3 and Fig. 4) but only tentative detections to the north and west, the source seems to be asymmetric. However, the estimated mass is in good agreement with the total mass derived from the OSO observations, which due to the larger beam cover the whole area of CO emission.

### 3.2. Molecular gas kinematics

The spectra in both maps (Fig. 7, 3, 4) clearly show two components, a fainter one (measured at the center) at  $v_{\text{lsr}} = 2690 \pm$

<sup>3</sup> full width of half maximum

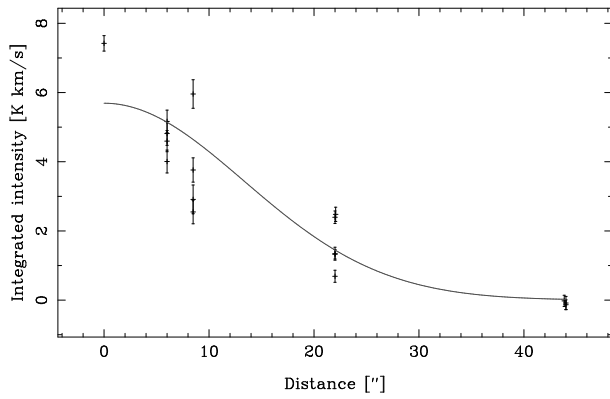


**Fig. 5.** The observed integrated intensities of  $^{12}\text{CO}(1-0)$  are plotted versus the distance from the central position. To estimate the molecular source size we fitted a Gaussian and determined the FWHM =  $22 \pm 1''$ .

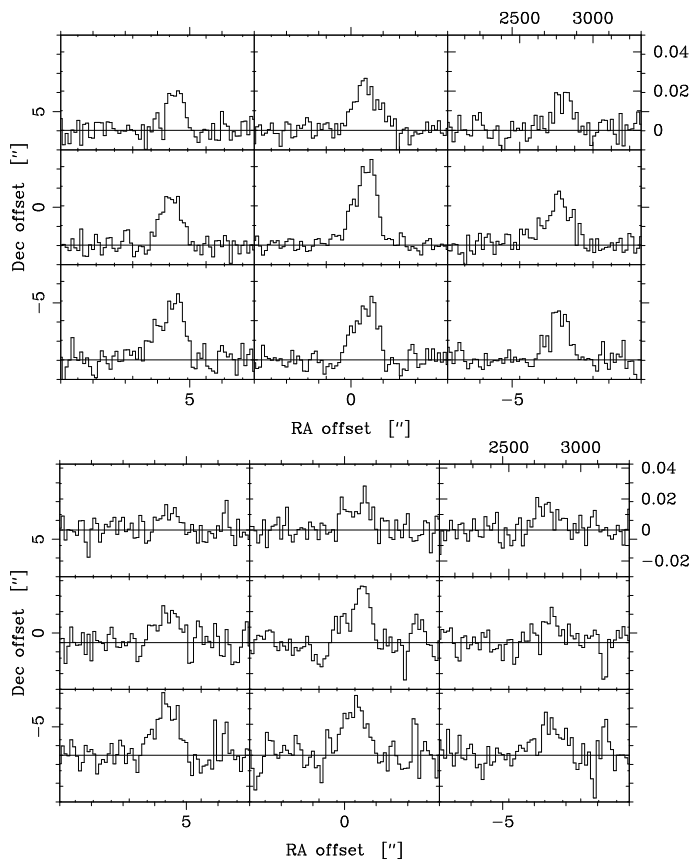


**Fig. 7.** Inner  $6'' \times 6''$  of the CO map observed with the IRAM 30 m telescope. The outer tick marks denote the spacing of the observed positions, the inner tick marks represent the velocity ( $\text{km s}^{-1}$ ) and  $T_{\text{MB}}$  (mK), respectively (labeled in the upper right spectrum). **top:**  $^{12}\text{CO}(1-0)$  map of the central region. Note that the data are highly oversampled (beamsize  $22''$ ). **bottom:**  $^{12}\text{CO}(2-1)$  map of the central region. Note that the data are close to being fully sampled (beamsize  $11''$ ). See Fig 3 and 4 for the larger scale maps.

$15 \text{ km s}^{-1}$  ( $2660 \pm 18 \text{ km s}^{-1}$  in  $^{12}\text{CO}(2-1)$ ) and the dominant one at  $v_{\text{LSR}} = 2790 \pm 10 \text{ km s}^{-1}$ . Comparing the spectra at individual positions, the relative intensities of both line components change, in particular in the SE direction. In the  $^{12}\text{CO}(2-1)$  map, the more blueshifted line is the brighter one at the offset posi-

tion ( $+15.6''$ ,  $-15.6''$ ) (see Fig. 4). This component is centered at  $2660 \text{ km s}^{-1}$  in  $^{12}\text{CO}(2-1)$  in each position, whereas in  $^{12}\text{CO}(1-0)$  there seems to be a slight shift from  $2690 \text{ km s}^{-1}$  in the center to  $2660 \text{ km s}^{-1}$  in the outer region.

Generally, the single dish molecular gas kinematics agrees with the overall central kinematics of the H I presented in Manthey et al. (2008a) in terms of the covered velocity range.

### 3.3. The nuclear region

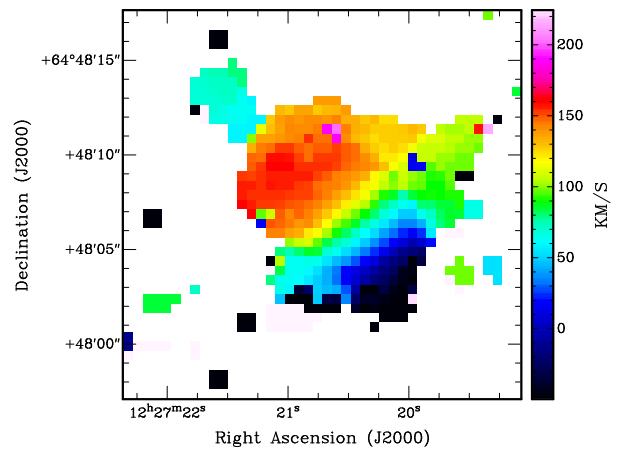
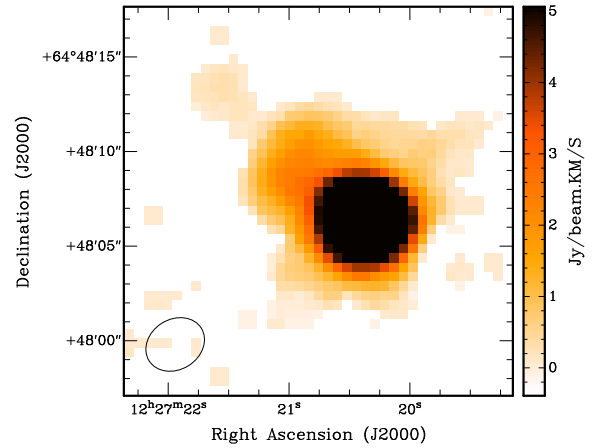


**Fig. 8.** Plateau de Bure maps of the central CO disc in NGC 4441: (top) the integrated intensity map, (bottom) the velocity map. The beam is shown in the lower left corner of the upper panel.

In Fig. 8 the integrated interferometer CO(1-0) intensity and velocity field maps of NGC 4441 are shown. Since interferometers filter out emission from extended diffuse gas, the maps show the distribution of fairly dense CO. We found what appears to be a small, inclined, nuclear disc aligned with the dust lane seen in

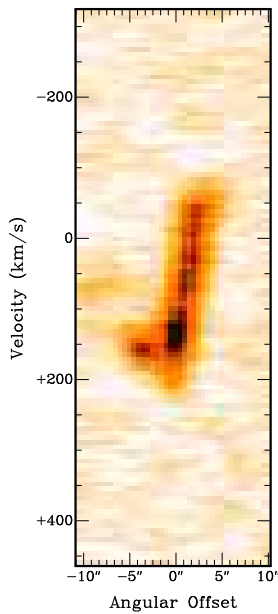


**Fig. 9.** pv-diagram along the major axis of the rotating CO disc. The position angle is  $PA=222^\circ$ , i.e. positive offsets are in south-western direction. The central velocity is  $2652 \text{ km s}^{-1}$ .

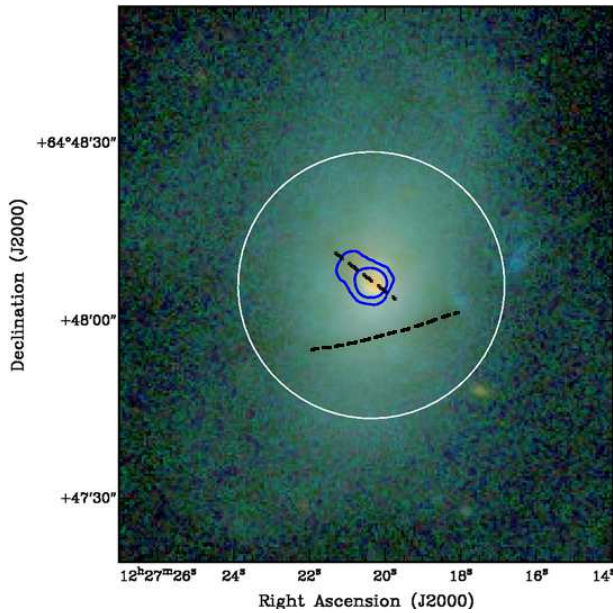


**Fig. 10.** SDSS *irg*-colour composite image of the main body of NGC 4441. Various dust lanes are visible. Overlaid are two contours of the CO distribution to highlight the extended and the compact component. The two dashed lines mark two dust lanes. Note that the central dust lane is associated with the molecular gas. This dust lane is broadened at the East side where a faint second peak in CO is seen. The white circle marks the primary beam of the Plateau de Bure interferometer.

the optical. The position angle of both the dust lane and the disc are identical. The orientation of the disc is northeast–southwest. Thus, it is inclined compared with the optical major axis. Most of the gas is concentrated around the optical nucleus. A second, fainter component with a small velocity dispersion is found north-east of the centre seen in Figs. 8,6 (‘hook’ in Fig. 9). This second peak is aligned with a broadened dust feature seen in the optical image (Fig. 10).

It is worth to note here that besides the central dust lane associated with the bulk of molecular gas, there are several faint off-centered dust lanes visible in optical images (e.g., south of the centre, Fig. 10). These lanes lie within the primary beam of the PdBI. Thus, if there was significant molecular gas also associated with these dust lanes, we would have detected it.

The total gas mass of the disc was calculated as  $M_{H_2} = 0.92 \cdot 10^4 \cdot F_{CO} \cdot D^2 = 4.1 \cdot 10^8 M_\odot$ , with  $D$  denoting the distance in Mpc,  $F$  being the integrated CO flux in  $\text{Jy km s}^{-1}$ . Thus, with the interferometric observations we detected  $\sim 87\%$  of the molecular gas mass seen in single-dish observations.

If we interpret the central feature as an inclined disc, its position-velocity diagram can be interpreted as the regular rotation pattern of a solid body (Figs. 8,9). The main parameters of this feature are given in Table 4. We calculated the dynamical mass of the nuclear disc with  $v_{\text{rot,max}} = 100 \text{ km s}^{-1}$  at a radius of  $R = 5'' = 875 \text{ kpc}$ . The disc appears to be close to edge-on, so we assume an inclination of  $i = 80^\circ$ . An error of  $\pm 10^\circ$  in inclination does not affect the result significantly. Thus, we calculate the dynamical mass as  $M_{\text{dyn}}(M_\odot) = R \cdot (v_{\text{rot,max}}/\sin i)^2 G^{-1} = 2.1 \cdot 10^9 M_\odot$ .

**Table 4.** Properties of the nuclear molecular gas feature found in NGC 4441.

property	value
size ("/kpc)	$10.3 \times 6.4 / 1.8 \times 1.1$
PA ( $^\circ$ )	222
$\Delta v$ ( $\text{km s}^{-1}$ )	295
$F_{CO}$ ( $\text{Jy km s}^{-1}$ )	29.1
$M_{\text{disc,H}_2}$ ( $M_\odot$ )	$4.1 \cdot 10^8$
$M_{\text{disc,dyn}}$ ( $M_\odot$ )	$2.1 \cdot 10^9$

### 3.4. $^{13}\text{CO}(1-0)$ and $^{13}\text{CO}(2-1)$

We also observed NGC 4441 in  $^{13}\text{CO}(1-0)$  and  $^{13}\text{CO}(2-1)$  at the center position. The  $^{13}\text{CO}(1-0)$  line is clearly detected, the  $^{13}\text{CO}(2-1)$  is only tentatively detected at a  $3\sigma$  level, but a feature at the expected velocity of  $2790 \text{ km s}^{-1}$  is found (see Fig. 11). Table 5 gives the linewidths and integrated intensities of all four lines at the center position. We fitted only one single Gaussian to the  $^{13}\text{CO}$  lines. The fitted center velocity of  $^{13}\text{CO}(1-0)$  (Table 5) lies between the derived values for the blue- and redshifted line using the  $^{12}\text{CO}$  transitions. In contrast, in  $^{13}\text{CO}(2-1)$  we see (if at all) the component with the higher velocity, which is also the stronger one in  $^{12}\text{CO}$  at the center. However, the signal-to-noise ratio of  $^{13}\text{CO}(2-1)$  is too low to draw firm conclusions.

In Table 6 the derived molecular gas mass and the molecular line intensity ratios based on the integrated intensities given in Table 5 are listed.

## 4. Radiative transfer calculations

To investigate the physical conditions of the ISM, we used RADEX<sup>4</sup> which is a one-dimensional spherically symmetric non-LTE radiative transfer code available on-line (van Langevelde & van der Tak 2004; Schöier et al. 2005; van der Tak et al. 2007). In this code, the mean escape probability method for an isothermal and homogeneous medium is used for the calculations.

<sup>4</sup> <http://www.strw.leidenuniv.nl/~moldata/radex.html>

**Table 6.** Integrated intensity line ratios derived from the CO measurements at the central position. In brackets the errors of the line ratio are given, following standard error propagation calculations. A source size of  $22''$  is used for the line ratios.

property	result
$M_{\text{H}_2}$ ( $10^8 M_{\odot}$ )	4.6
$^{12}\text{CO}(2-1)/^{12}\text{CO}(1-0)$	0.5 (0.06)
$^{13}\text{CO}(2-1)/^{13}\text{CO}(1-0)$	0.42 (0.17)
$^{12}\text{CO}(1-0)/^{13}\text{CO}(1-0)$	21 (3.5)
$^{12}\text{CO}(2-1)/^{13}\text{CO}(2-1)$	25 (7.6)

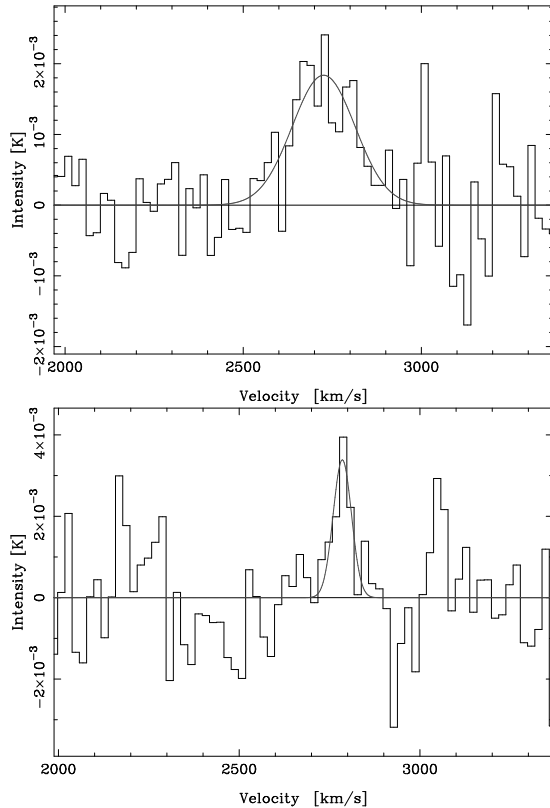


**Fig. 11.**  $^{13}\text{CO}$  observed at the center position of NGC 4441, measured with the IRAM 30 m telescope. The intensity is given in units of  $T_{\text{MB}}$ . **top:**  $J=1-0$ ,  $\text{rms}=0.7$  mK. **bottom:**  $J=2-1$ ,  $\text{rms}=1.3$  mK. Overlaid are Gaussian fits to the lines. The parameters are given in Table 5.

We assume that the  $^{12}\text{CO}$  lines are optically thick ( $\tau > 1$ ), so that the CO is selfshielded from the UV radiation field. The high  $^{12}\text{CO}/^{13}\text{CO}$  line ratio limits the optical depths to  $\tau < 10$ , unless the  $^{13}\text{CO}$  abundances are extraordinarily low. Furthermore, we assume “standard” abundances of  $^{12}\text{CO}$  and  $^{13}\text{CO}$  of  $X[^{12}\text{CO}] = 10^{-4}$  and  $X[^{13}\text{CO}] = 2 \cdot 10^{-6}$  (e.g., Blake et al. 1987; Mao et al. 2000). The line ratios fitted by the radiative transfer model constrain the average properties of an ensemble of clouds that are not filling the beam. We are assuming that the emission is emerging from a single cloud type - which in reality is very unlikely to be true, but provides us with a first handle on the main properties of the  $^{12}\text{CO}/^{13}\text{CO}$  emitting gas.

We explore a range of  $\text{H}_2$  column densities and temperatures of  $10^{18} - 10^{22} \text{ cm}^{-2}$  and  $10 - 50$  K. In Fig. 12 the results for  $\text{H}_2$  column densities of  $10^{20} \text{ cm}^{-2}$  and  $10^{21} \text{ cm}^{-2}$  are displayed. The levels decrease from high temperatures at low densities to low temperatures at high densities. The measured line ratios  $^{12}\text{CO}(2-$

$1)/^{12}\text{CO}(1-0)$  and  $^{13}\text{CO}(2-1)/^{13}\text{CO}(1-0)$  both indicate subthermally excited emission, i.e., either low temperatures and/or low density.

The best agreement of the  $^{12}\text{CO}(2-1)/^{12}\text{CO}(1-0)$  and  $^{13}\text{CO}(2-1)/^{13}\text{CO}(1-0)$  lines ratios is found for a column density per cloud of  $10^{21} \text{ cm}^{-2}$ .

From the  $^{12}\text{CO}$  and  $^{13}\text{CO}$  ratios alone it is not possible to determine the temperature in a more specific way, but as seen in Fig. 12, for higher temperatures ( $> 20$  K) the density is well below  $1000 \text{ cm}^{-3}$ . There are no signs of warm, dense ( $n > 10^4 \text{ cm}^{-3}$ ) cores. For the gas to be dense and still fit the observed line ratios, temperatures of 5 K are required, which is significantly lower than the dust temperature. This is of course technically possible, but such a cold dense component would quickly collapse and form stars. We find it more likely that the observed line ratios indicate a low density ( $n < 1000 \text{ cm}^{-3}$ ) molecular ISM where the clouds are diffuse — i.e. not entirely self-gravitating — or consisting of extended outskirts of much smaller, bound clouds. This would be in agreement with the moderate to low star formation rate derived for NGC 4441 (Manthey et al. 2008a).

Interestingly, the  $^{12}\text{CO}/^{13}\text{CO}$  line ratio in NGC 4441 is unusually high for a galaxy with a moderate to low star formation rate. Values found here are more reminiscent of starburst nuclei (15–20) (Aalto et al. 1995).

It is possible that the ISM in NGC 4441 is the left-over from a burst of star formation that consumed the denser fraction of the gas. Diffuse gas may also be the result of dynamical impact on the gas properties: tidal forces, bar-induced shocks or the merger event.

## 5. Discussion

### 5.1. A counter-rotating nuclear molecular disc?

Nuclear rotating discs are often found in interacting galaxies (e.g., Bryant & Scoville 1996; Downes & Solomon 1998; Bryant & Scoville 1999; Yun & Hibbard 2001). Even though these studies concentrate on ULIRGs, some of the observed features are similar to the disc found in NGC 4441. The discs found in mergers of spirals are very compact, with typical radii of 300–800 pc. Furthermore, the molecular gas fraction traced by CO tends to have a rather low density ( $10^2 - 10^3 \text{ cm}^{-3}$ ) (Downes & Solomon 1998). Therefore, the CO lines are subthermally excited (Downes & Solomon 1998), as we also assume for NGC 4441. However, in ULIRGs turbulence is rather high (up to  $100 \text{ km s}^{-1}$ , (e.g., Downes & Solomon 1998)) which explains why gravitational instabilities occur leading to the observed high star formation rate. The ISM in the nuclear disc of NGC 4441 might be less turbulent due to a different merger history. If NGC 4441 is a S+E merger, only one partner brings in a significant amount of molecular gas, which might form an interaction-triggered disc more smoothly. Therefore, the disc might be more stable and thus only moderate ongoing star formation is observed.

Besides the diffuse component generally found in ULIRGs, the bulk of the molecular gas is in a dense phase ( $10^5 - 10^6 \text{ cm}^{-3}$ ), supporting the extreme star formation (e.g., Solomon et al. 1992; Greve et al. 2006). Based on our radiative transfer modelling we find no hints of such a dominant dense gas phase in NGC 4441, in accordance to the moderate star formation rate.

Compared with the rotation of the large-scale HI disc (Manthey et al. 2008a), the nuclear molecular disc is kinematically decoupled. Its rotation axis is shifted by  $\sim 100^\circ$ .

Kinematically decoupled cores (KDCs) are found in various galaxies, in spirals as well as in S0 and ellipticals (e.g., Krajnović et al. 2008; Haynes et al. 2000; Kuijken et al. 1996). First simulations of Hernquist & Barnes (1991) showed that counter-rotating nuclear discs can occur in an equal-mass disc-disc merger in which the two progenitors have anti-parallel spins (i.e., a *retrograde* merger). In this scenario, the nuclear disc contains gas from the centres of the original gas discs which was exposed to strong gravitational torques and thus losing most of the angular momentum. Because of that, no information about the original sense of rotation is preserved and thus the rotation axis of the new disc is not related to the original ones. In contrast, the gas in the outer parts can retain its angular momentum and thus conserves the original motion. In this scenario, the merger remnants evolve into elliptical galaxies which are often found to host a KDC.

Further theoretical studies showed that KDCs in S0 and spirals can occur due to minor mergers with gas rich companions, and even mergers with at least one elliptical can lead to (stellar) KDCs (e.g., Bertola & Corsini 1999; Thakar & Ryden 1998; Haynes et al. 2000; di Matteo et al. 2008). Besides the variety of merging partners leading to a KDC, all simulations have in common that the merger geometry has to be retrograde.

### 5.1.1. Is the minor axis dust lane really an inclined disc?

The interpretation of the crossing central dust lane of NGC 4441 as an inclined disc seems likely due to the large velocity shift along the lane as well as the regular-looking shape of the associated  $p\nu$  diagram. The disc appears stable against star formation and may be filled with diffuse, unbound molecular gas. However, one problem is the apparent counter-rotation of the inclined disc. In our previous paper on H I (Manthey et al. 2008a) we suggested that the interaction between the two galaxies was pro-grade, because of a large amount of angular momentum still remaining in the gas of the tidal tails. However, retrograde mergers appear to be a requirement to produce counter-rotating cores. If the pro-grade scenario were correct, there is a problem with the interpretation of the dust lane as an inclined disc. A final answer cannot be given by these observations alone but is only possible by obtaining numerical simulations.

Minor axis dust lanes in other E+S mergers (such as Cen-A, Fornax-A, NGC 4194 (the Medusa)) present a variety of dynamical behaviour. In the Medusa the dust lane is morphologically similar to the one in NGC 4441, but has a much smaller velocity gradient and is not interpreted as a disc, but rather as a lane along which gas is fed to the nucleus (Aalto & Hüttemeister 2000). In NGC 4441, however, we do not find such a central starburst.

## 5.2. Present state and expected future evolution of NGC 4441

The presence of an extended molecular gas reservoir in NGC 4441 is comparable to what is found in NGC 4194, the prototypical S+E merger candidate (Aalto & Hüttemeister 2000). However, the geometry compared to the optical appearance is different. In the Medusa the CO follows roughly the direction of the optical tidal tail, whereas in NGC 4441 the molecular gas seems to be more extended to the opposite side of the optical tail. This is probably a result of a different merger geometry of these two galaxies. In any case, extended molecular gas indicates a different merger history compared to ULIRGs in which molecular gas is concentrated in the central kpc. Based on the simi-

lar optical morphology, in particular the strength of the features, it seems likely that NGC 4441 and NGC 4194 are in a similar merger state.

Interestingly, the molecular gas mass of NGC 4441 is only a quarter of the Medusa ( $4.6 \cdot 10^8 M_{\odot}$  for NGC 4441), whereas the amount of atomic hydrogen is comparable ( $1.46 \cdot 10^9 M_{\odot}$  in NGC 4441 versus  $2 \cdot 10^9 M_{\odot}$  in the Medusa) (Manthey et al. 2008a,b). The question arises, why the starburst in NGC 4441 has already faded, while the Medusa is still intensely forming stars. The relation between the ongoing star formation and the available resource for star formation (i.e., dense gas) can be expressed by the star formation efficiency:  $\text{SFE}(\frac{\text{yr}}{\text{yr}}) = \frac{\text{SFR}_{\text{FIR}}}{M_{\text{H}_2}}$ . Thus, for NGC 4441 we derive a star formation efficiency of  $\text{SFE} = 2.1 \cdot 10^{-9} \text{yr}^{-1}$ . The equivalent gas depletion time is  $\tau = 1/\text{SFE} = 4.8 \cdot 10^8 \text{yr}$ . If we assume a conversion factor  $X_{\text{CO}}$  to be similar as in the Medusa, we can directly compare the SFE with that in NGC 4194, because their metallicities are similar (Jütte et al. 2009; Arimoto et al. 1996). Comparing NGC 4441 with the very effective star burst in the Medusa (up to an efficiency of  $1.7 \cdot 10^{-8} \text{yr}$  (Aalto & Hüttemeister 2000)), NGC 4441 has a moderate star formation efficiency:  $\text{SFE}(\text{NGC 4194}) \sim 10 \times \text{SFE}(\text{NGC 4441})$ . Since the  $\text{H}_2$ -to-CO conversion factor might be different for starbursting and 'quiescent' galaxies, we may overestimate the mass, and therefore underestimate the SFE in comparison with the Medusa. But these dependencies are not well understood so far and can't be taken into account here. From the radiative transfer models, we find that the molecular gas is rather thin and cold in NGC 4441, which makes it difficult to form new stars, whereas in the Medusa the CO lines are thermalised, indicating higher average gas densities and/or temperatures. It is, however, unclear, whether the differences are due to ageing effects, e.g., NGC 4441 might have transformed all dense gas into stars, whereas in the Medusa this process is still ongoing. Furthermore, differences in the gas densities can be explained by different gas reservoirs provided by the progenitors and/or different merger geometry.

Thus, if this galaxy is already in a post-starburst phase, it still manages to retain a large amount of gas in principle available for star formation.

This is in agreement with observations of so-called 'E+A' galaxies, i.e. post-starburst with an optical spectrum reflecting a strong A star population superimposed on an old elliptical-like population. A small but significant fraction of E+A galaxies have optical tidal features, suggesting a merger event only 0.5–1 Gyr ago (e.g., Zabludoff et al. 1996; Blake et al. 2004). Furthermore, Buyle et al. (2006) obtained HI observations of a sample of E+A galaxies and show that the total atomic gas content may not be consumed until a galaxy reaches that post-starburst phase.

Furthermore, a large amount of diffuse molecular gas can survive a starburst phase (Kohno et al. 2002), when the gas in the dense cores is consumed during the star formation process. It is argued by Kohno et al. (2002) that the remaining molecular gas can be stable against gravitational instabilities. Such instabilities could lead to a condensation and thus trigger star formation. In particular in early-type galaxies such as NGC 4441, the mass density increases steeply towards the center, which leads to a rise of the rotation velocity. Therefore, the epicyclic frequency, which is proportional to the critical mass density, also rises and hence also the critical mass density, which is the lower threshold density for possible star formation. In other words, the star formation is suppressed, although raw material is still present in the galaxy.

Indeed, the small regularly rotating central molecular gas feature

which is likely a disc, seems to be stable, i.e., not star forming and thus is similar to what is found in NGC 5195 by Kohno et al. (2002).

## 6. Summary

1. We observed the advanced merger remnant NGC4441 in  $^{12}\text{CO}(1-0)$  using the Onsala 20 m telescope. We determined a total molecular gas mass of  $4.6 \cdot 10^8 M_{\odot}$ .
2. The star formation efficiency is  $2.1 \cdot 10^{-9} \text{ yr}^{-1}$  and the gas depletion time  $\tau = 4.8 \cdot 10^8 \text{ yr}$ .
3. Following up, we mapped NGC 4441 with the single-dish IRAM 30 m telescope in  $^{12}\text{CO}(1-0)$  and  $^{12}\text{CO}(2-1)$ . We found extended molecular gas out to  $22''$  (3.9 kpc).
4. Two distinct velocity components with a velocity difference of  $\sim 100 \text{ km s}^{-1}$  were detected. The relative intensities of both components vary with distance from the center and with transition.
5. High resolution imaging using Plateau de Bure revealed a small central rotating molecular gas disc hosting most of the molecular gas in NGC 4441. In contrast to ULIRGs, which also have compact molecular gas disc fueling the central superstarburst, the disc in NGC 4441 seems to be stable and thus does not support star formation.
6. The central molecular gas disc has a different sense of rotation than the large-scale H I distribution. This is a strong indicator of a kinematically decoupled core.
7. Furthermore, we observed the  $^{13}\text{CO}(1-0)$  and  $^{13}\text{CO}(2-1)$  line with the IRAM 30 m telescope to estimate the molecular gas properties using the radiative transfer model RADEX. We derived  $^{12}\text{CO}(2-1)/^{12}\text{CO}(1-0)$  and  $^{13}\text{CO}(2-1)/^{13}\text{CO}(1-0)$  line ratios which are consistent with a diffuse ( $n_{\text{H}_2} \leq 1000 \text{ cm}^{-3}$ ) molecular medium. However, the  $^{12}\text{CO}(1-0)/^{13}\text{CO}(1-0)$  ratio is unusually high ( $^{12}\text{CO}(1-0)/^{13}\text{CO}(1-0) = 21$ ), which is typical for the inner centers of luminous starbursts (Aalto et al. 1995).
8. The moderate star formation rate of  $1-2 M_{\odot} \text{ yr}^{-1}$  is in good agreement with the results from the molecular gas analysis. Because not much dense ( $n \geq 10^4 \text{ cm}^{-3}$ ) gas is present, no enhanced ongoing star formation can happen. The strength of a past starburst remains unclear, however.
9. NGC 4441 may be a local candidate for an E+A galaxy, still hosting a significant amount of gas but the starburst has been faded away already.

*Acknowledgements.* We thank Evert Olsson for his assistance of the IRAM observations. We thank the Onsala Space Observatory, and IRAM staff for their support during the observations. This research has made use of the NASA/IPAC Extragalactic Database (NED) which is operated by the Jet Propulsion Laboratory, California Institute of Technology, under contract with the National Aeronautics and Space Administration. The research was partially supported by the German Science Organisation (DFG) through the Graduiertenkolleg 787.

## References

Aalto, S., Booth, R. S., Black, J. H., & Johansson, L. E. B. 1995, A&A, 300, 369  
 Aalto, S. & Hüttemeister, S. 2000, A&A, 362, 42  
 Aalto, S., Hüttemeister, S., & Polatidis, A. G. 2001, A&A, 372, L29  
 Arimoto, N., Sofue, Y., & Tsujimoto, T. 1996, PASJ, 48, 275  
 Bergvall, N. 1981, A&A, 97, 302  
 Bertola, F. & Corsini, E. M. 1999, in IAU Symposium, Vol. 186, Galaxy Interactions at Low and High Redshift, ed. J. E. Barnes & D. B. Sanders, 149–+  
 Blake, C., Pracy, M. B., Couch, W. J., et al. 2004, MNRAS, 355, 713  
 Blake, G. A., Sutton, E. C., Masson, C. R., & Phillips, T. G. 1987, ApJ, 315, 621  
 Braine, J. & Combes, F. 1992, A&A, 264, 433

Braine, J. & Combes, F. 1993, A&A, 269, 7  
 Bryant, P. M. & Scoville, N. Z. 1996, ApJ, 457, 678  
 Bryant, P. M. & Scoville, N. Z. 1999, AJ, 117, 2632  
 Buyle, P., Michielsen, D., De Rijcke, S., et al. 2006, ApJ, 649, 163  
 de Vaucouleurs, G., de Vaucouleurs, A., Corwin, H. G., et al. 1995, VizieR Online Data Catalog, 7155, 0  
 di Matteo, P., Combes, F., Melchior, A.-L., & Semelin, B. 2008, A&A, 477, 437  
 Downes, D. & Solomon, P. M. 1998, ApJ, 507, 615  
 Dupraz, C. & Combes, F. 1985, Lecture Notes in Physics, Berlin Springer Verlag, 232, 151  
 Greve, T. R., Papadopoulos, P. P., Gao, Y., & Radford, S. J. E. 2006, ArXiv Astrophysics e-prints  
 Haynes, M. P., Jore, K. P., Barrett, E. A., Broeils, A. H., & Murray, B. M. 2000, AJ, 120, 703  
 Hernquist, L. & Barnes, J. E. 1991, Nature, 354, 210  
 Horellou, C. & Booth, R. 1997, A&AS, 126, 3  
 Jütte, E., Jütte, M., Hüttemeister, S., & Aalto, S. 2009, in prep.  
 Khochfar, S. & Burkert, A. 2003, ApJ, 597, L117  
 Kohno, K., Tosaki, T., Matsushita, S., et al. 2002, PASJ, 54, 541  
 Kojima, M. & Noguchi, M. 1997, ApJ, 481, 132  
 Krajnović, D., Bacon, R., Cappellari, M., et al. 2008, MNRAS, 390, 93  
 Kuijken, K., Fisher, D., & Merrifield, M. R. 1996, MNRAS, 283, 543  
 Manthey, E., Aalto, S., Hüttemeister, S., & Oosterloo, T. A. 2008a, A&A, 484, 693  
 Manthey, E., Hüttemeister, S., Aalto, S., Horellou, C., & Bjerkeli, P. 2008b, A&A, 490, 975  
 Manthey, E., Hüttemeister, S., Haberbzettel, L., & Aalto, S. 2005, in AIP Conf. Proc. 783: The Evolution of Starbursts, ed. S. Hüttemeister, E. Manthey, D. Bomans, & K. Weis, 343–348  
 Mao, R. Q., Henkel, C., Schulz, A., et al. 2000, A&A, 358, 433  
 Naab, T. & Burkert, A. 2000, in ASP Conf. Ser. 197: Dynamics of Galaxies: from the Early Universe to the Present, ed. F. Combes, G. A. Mamon, & V. Charmandaris, 267  
 Naab, T. & Burkert, A. 2001, in ASP Conf. Ser. 230: Galaxy Disks and Disk Galaxies, ed. J. G. Funes & E. M. Corsini, 453–454  
 Naab, T., Jesseit, R., & Burkert, A. 2006, MNRAS, 372, 839  
 Quinn, P. J. 1984, ApJ, 279, 596  
 Sanders, D. B. & Mirabel, I. F. 1996, ARA&A, 34, 749  
 Schöier, F. L., van der Tak, F. F. S., van Dishoeck, E. F., & Black, J. H. 2005, A&A, 432, 369  
 Solomon, P. M., Downes, D., & Radford, S. J. E. 1992, ApJ, 387, L55  
 Steinmetz, M. 2003, Ap&SS, 284, 325  
 Strong, A. W., Bloemen, J. B. G. M., Dame, T. M., et al. 1988, A&A, 207, 1  
 Thakar, A. R. & Ryden, B. S. 1998, ApJ, 506, 93  
 van der Tak, F. F. S., Black, J. H., Schöier, F. L., Jansen, D. J., & van Dishoeck, E. F. 2007, A&A, 468, 627  
 van Langevelde, H. J. & van der Tak, F. 2004, <http://www.strw.leidenuniv.nl/moldata/radex.html>  
 Weil, M. L. & Hernquist, L. 1993, ApJ, 405, 142  
 Weistrop, D., Eggers, D., Hancock, M., et al. 2004, AJ, 127, 1360  
 Yun, M. S. & Hibbard, J. E. 2001, ApJ, 550, 104  
 Zabludoff, A. I., Zaritsky, D., Lin, H., et al. 1996, ApJ, 466, 104

**Table 3.** CO line parameters of the map of NGC 4441. The reference coordinates are the center coordinates (J2000): RA:  $12^{\text{h}}27^{\text{m}}20.36^{\text{s}}$ , DEC:  $+64^{\circ}48'06''$ . Given are the offset positions, the total velocity range of the CO(1-0) and CO(2-1) line and the intensities of both lines. The temperatures are measured in  $T_{\text{MB}}$ .

$\Delta$ RA (")	$\Delta$ DEC (")	$\text{rms}_{\text{CO}(1-0)}$ (mK)	$\Delta v_{\text{CO}(1-0)}$ ( $\text{km s}^{-1}$ )	$I_{\text{CO}(1-0)}$ ( $\text{K km s}^{-1}$ )	$\text{rms}_{\text{CO}(2-1)}$ (mK)	$\Delta v_{\text{CO}(2-1)}$ ( $\text{km s}^{-1}$ )	$I_{\text{CO}(2-1)}$ ( $\text{K km s}^{-1}$ )
0	0	2.50	292	7.52	7.67	324	6.10
6	6	4.62	283	2.34	6.72	240	1.84
0	6	3.43	328	4.80	6.34	270	3.51
-6	6	5.33	209	2.68	5.95	252	2.69
6	0	3.78	267	4.24	7.67	302	3.64
-6	0	3.86	336	1.69	7.67	247	2.50
6	-6	5.28	344	6.65	7.87	220	6.34
0	-6	3.75	320	4.60	9.6	285	6.14
-6	-6	4.42	259	3.70	9.6	308	3.97
0	22	2.19	220	0.92	3.62	–	–
-22	0	2.06	–	1.67	2.88	–	–
0	-22	1.64	262	1.44	3.07	–	–
22	0	2.33	316	2.47	2.30	275	0.88
15.6	-15.6	2.39	310	2.53	2.11	318	2.23
44	0	1.77	–	–	3.07	–	–
0	-44	2.18	–	–	2.11	–	–
31	-31	2.00	–	–	2.88	–	–

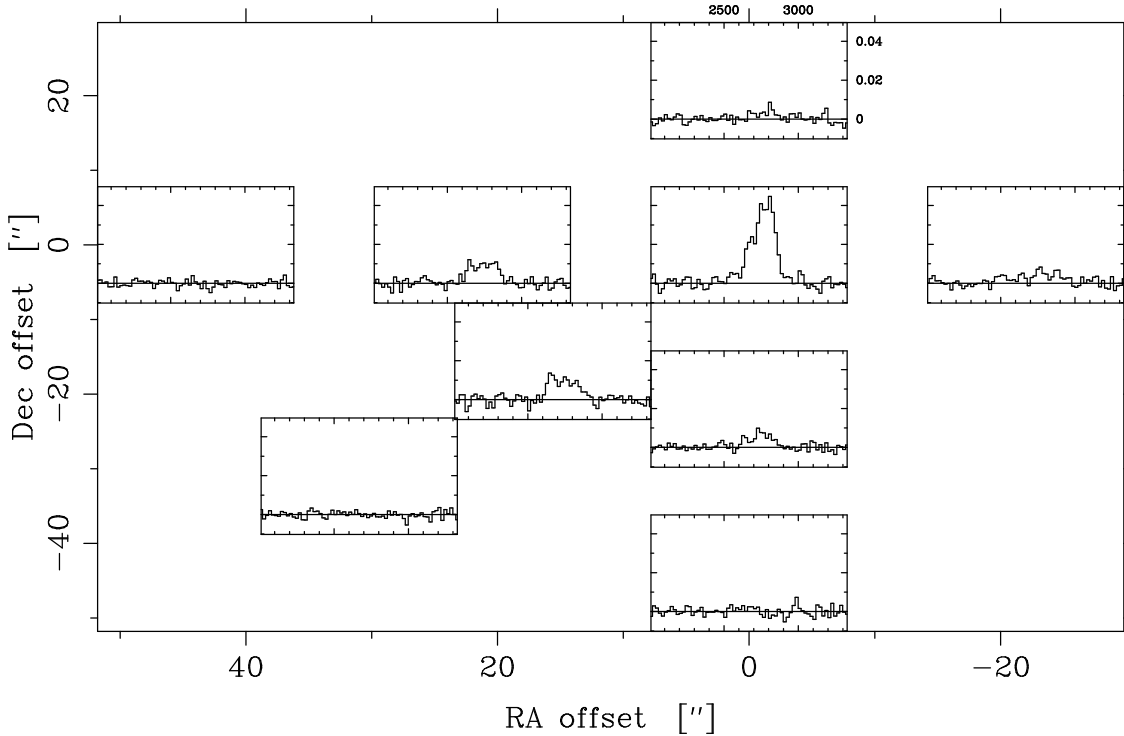


**Fig. 3.** Large  $^{12}\text{CO}(1-0)$  map of NGC 4441, observed with the IRAM 30 m telescope. The outer tick marks denote the spacing of the observed positions, the inner tick marks represent the velocity ( $\text{km s}^{-1}$ ) and  $T_{\text{MB}}$  (mK), respectively.

**Table 5.** Parameters of  $^{12}\text{CO}$  and  $^{13}\text{CO}$  at the central position. Gaussians were fitted to determine linewidths, peak intensity and center velocity. For  $^{12}\text{CO}$ , we fitted two components to the measured line, in  $^{13}\text{CO}$  only one component was fitted. The given intensity is integrated over both components. Temperatures are given in  $T_{\text{MB}}$ .

line	center velocity (lsr)		linewidth ( $\text{km s}^{-1}$ )		Peak (K)		int. Intensity ( $\text{K km s}^{-1}$ )
$^{12}\text{CO}(1-0)$	2698	2796	125	147	0.02	0.036	$7.52 \pm 0.22$
$^{12}\text{CO}(2-1)$	2655	2802	93	114	0.016,	0.039	$6.10 \pm 0.73$
$^{13}\text{CO}(1-0)$		2725		208		0.0018	$0.37 \pm 0.06$
$^{13}\text{CO}(2-1)$		2785		61		0.0033	$0.25 \pm 0.09$

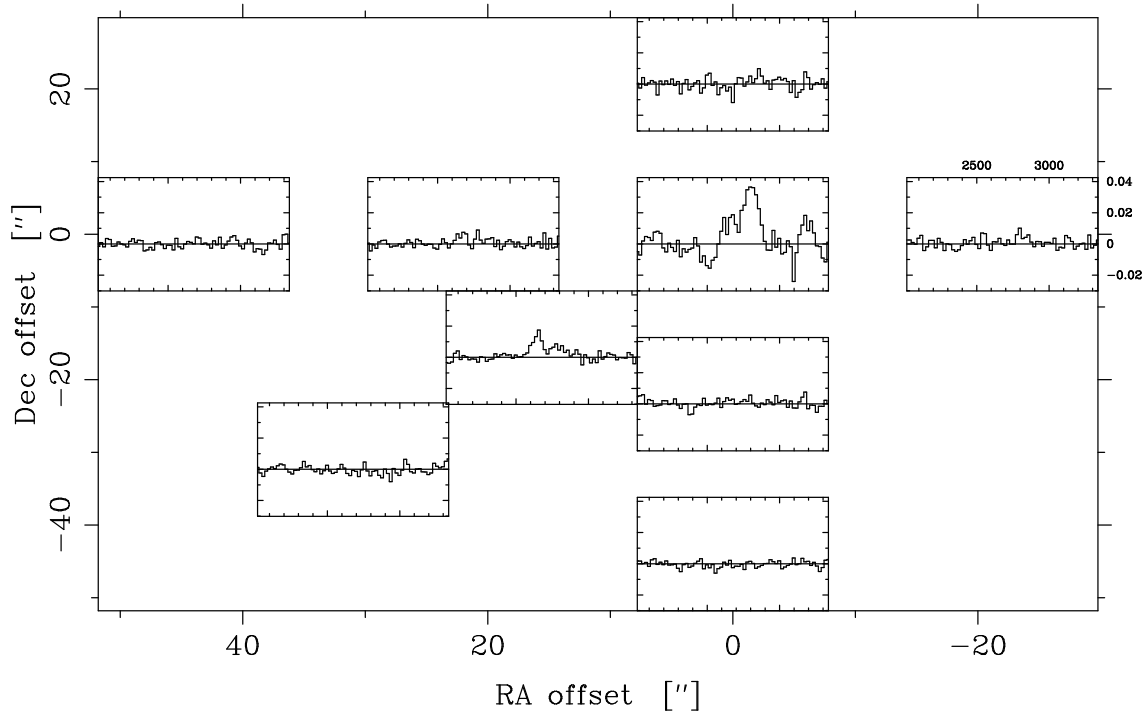


**Fig. 4.** Large  $^{12}\text{CO}(2-1)$  map of NGC 4441, observed with the IRAM 30 m telescope. The outer tick marks denote the spacing of the observed positions, the inner tick marks represent the velocity (km s $^{-1}$ ) and  $T_{\text{MB}}$  (mK), respectively.

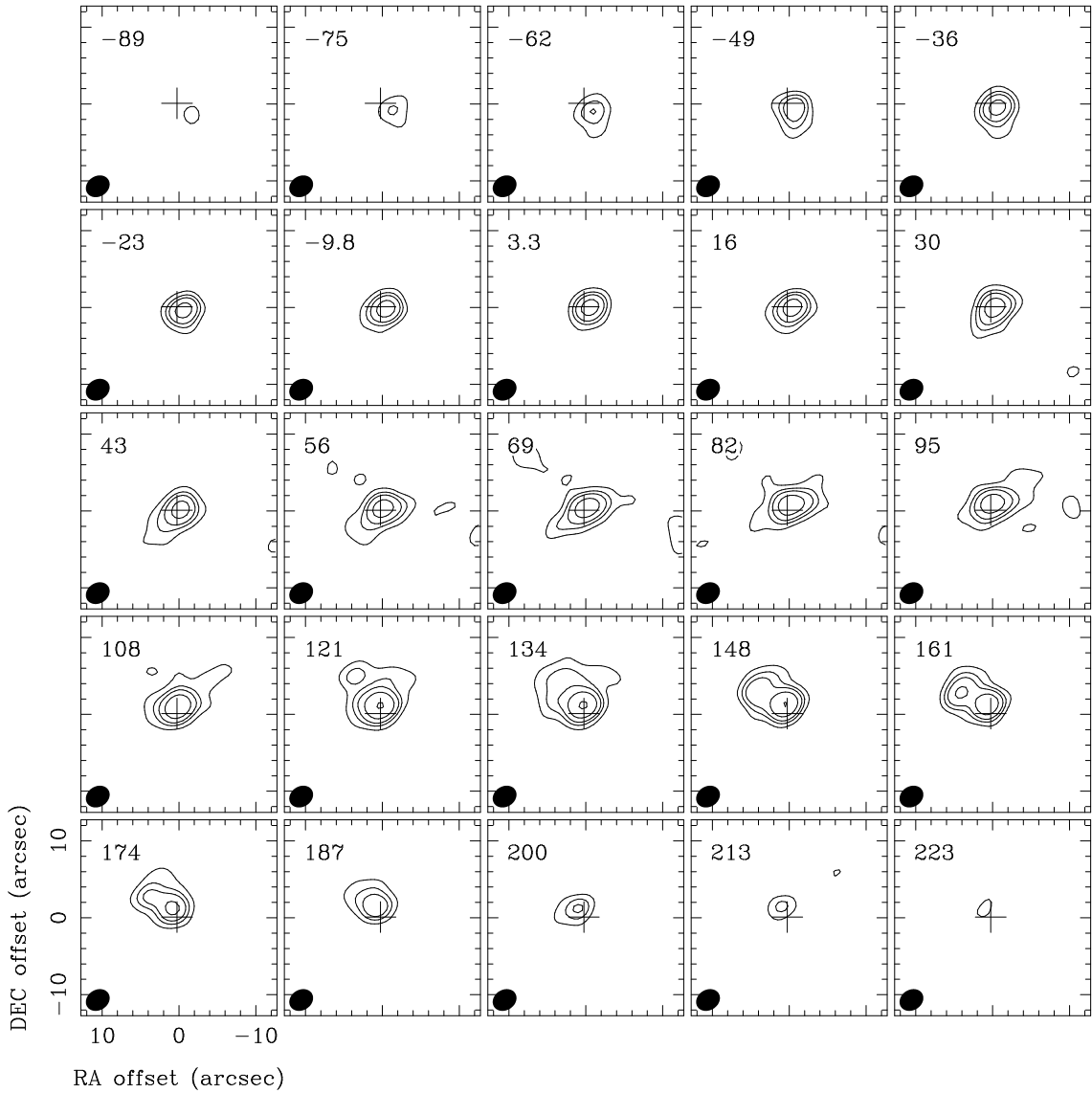


**Fig. 6.** Channel maps of the nuclear rotating molecular gas disc observed with the Plateau de Bure interferometer. The contours are 1, 2, 3, 5, 10,  $15 \cdot 0.01\text{Jy beam}^{-1}$ . The central velocity is  $2652 \text{ km s}^{-1}$ .

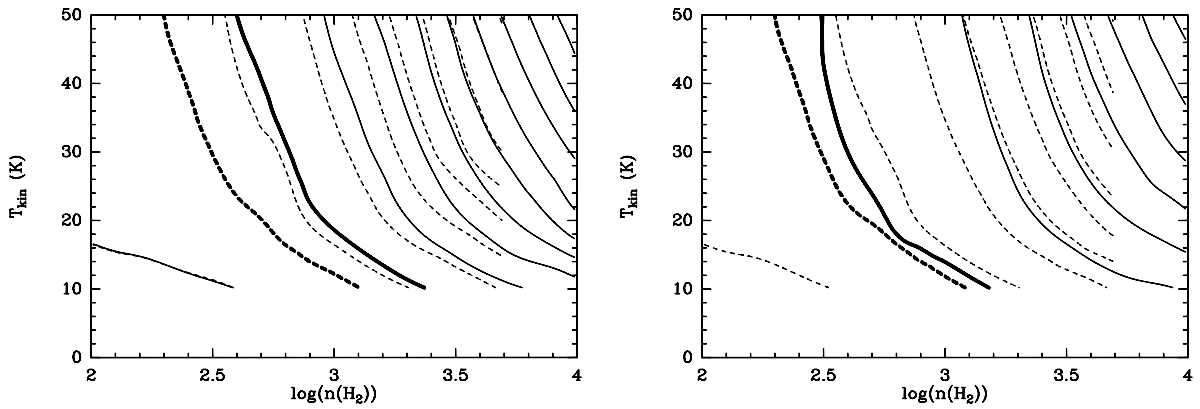


**Fig. 12.** Results of the RADEX analysis. The  $\text{H}_2$  column density is  $10^{20} \text{ cm}^{-2}$  (right), and  $10^{21} \text{ cm}^{-2}$ . Shown are the line ratios of  $^{12}\text{CO}(2-1)/^{12}\text{CO}(1-0)$  (solid) and  $^{13}\text{CO}(2-1)/^{13}\text{CO}(1-0)$  (dashed). The bold lines mark the measured line ratios of NGC 4441. The levels of the line ratios start at 0.25 and proceed in steps of 0.25. For this analysis, we assumed a linewidth of  $10 \text{ km s}^{-1}$  per cloud and abundances of  $X[^{12}\text{CO}] = 10^{-4}$  and  $X[^{13}\text{CO}] = 2 \cdot 10^{-6}$ .